JOURNAL OF PROPULSION AND POWER
Vol. 15, No. 1, January–February 1999

Simulation and Optimization of Heated, Inviscid Flows in Scramjet Ducts

Peter A. Jacobs* and Chris S. Craddock†
University of Queensland, Brisbane, Queensland, 4072, Australia

A space-marching code for the simulation and optimization of inviscid supersonic flow in three dimensions is described. The flow in a scramjet module with a relatively complex three-dimensional geometry is examined and wall-pressure estimates are compared with experimental data. Given that viscous effects are not presently included, the comparison is reasonable. The thermodynamic compromise of adding heat in a diverging combustor is also examined. The code is then used to optimize the shape of a thrust surface for a simpler (box-section) scramjet module in the presence of uniform and nonuniform heat distributions. The optimum two-dimensional profiles for the thrust surface are obtained via a perturbation procedure that requires about 30–50 flow solutions. It is found that the final shapes are fairly insensitive to the details of the heat distribution.

Nomenclature

A	= cross-sectional area of duct, m^2
a	= local speed of sound, m/s
C_p	= heat capacity (constant P), J/(kg K)
C_v	= heat capacity (constant V), J/(kg K)
E	= total energy (internal + kinetic), J/kg
e	= specific internal energy, J/kg
$\bar{F}$	= vector of fluxes
I_{sp}	= specific impulse, s
$\hat{i}, \hat{j}, \hat{k}$	= unit vectors in Cartesian coordinates
M	= Mach number
$\hat{n}$	= unit normal vector for a cell face
P	= pressure, Pa
$\bar{P}$	= position vector
Q	= algebraic vector of source terms
q	= heating per unit volume, J/(m^3 s)
R	= gas constant, J/(kg K)
S	= control surface of the cell
s	= entropy, J/(kg K)
T	= temperature, K
t	= time, s
U	= algebraic vector of conserved quantities
u	= velocity, m/s
V	= volume, m^3
x, y, z	= Cartesian coordinates, m
γ	= ratio of specific heats
ξ, η, ζ	= normalized coordinates
ρ	= density, kg/m^3

Subscripts

A, B, C, D	= vertex labels
ix, iy, iz	= cell-center indices
$ix \pm 1/2$	= vertical, streamwise interface
$iy \pm 1/2$	= horizontal interface
$iz \pm 1/2$	= vertical, cross-stream interface
x, y, z	= Cartesian components

Superscripts

T	= transpose
$'$	= pertaining to the upstream vertex slice

Received April 5, 1996; revision received June 25, 1998; accepted for publication July 2, 1998.

*Lecturer, Department of Mechanical Engineering.
†Graduate Student, Department of Mechanical Engineering.

Introduction

SUPERSONIC combustion ramjets (scramjets) have been studied at the University of Queensland, Australia, for 15 years and, although the concept of a scramjet is simple, the goal of producing and flight testing a scramjet-powered vehicle has proved elusive. Part of the motivation for pursuing scramjet technology is the scaling argument put forward by Stalker.[1] His study suggested that a small launch vehicle, with a scramjet-powered second stage and the capability of placing a 1000-kg payload into low Earth orbit, can be operated competitively against traditional, all-rocket launch vehicles. The trajectory of the scramjet stage needs to be low and through a relatively dense part of the atmosphere because the atmospheric air is required to burn the fuel. This will result in the scramjet vehicle experiencing larger aerothermodynamic loads than a conventional rocket. However, with the scramjet having a relatively low drag coefficient and a small volume, there may be a significant advantage to using a scramjet stage.

The design for the scramjet stage used in this study was based on the accelerator vehicle studied by NASA.[2] It is an axisymmetric vehicle with a conical forebody and a set of six scramjet modules surrounding the centerbody as shown in Fig. 1. Each module was based on a strutless version of the NASA Langley Research Center's parametric scramjet module.[3] Recent tests on a small-scale model[4] have demonstrated that a net thrust can be developed in the high-enthalpy flow of a shock tunnel, but many of the issues of building a scramjet-powered vehicle for free flight have yet to be resolved.

To address some of the issues of building flight-style scramjet modules, a combined experimental and computational study was undertaken. The experimental component of the study involved the construction and testing of a sequence of three module designs within the T4 shock tunnel.[5] The final composite scramjet motor (CSM) was fabricated from fiber-composite materials and had a fully three-dimensional geometry. The relatively complex geometry of the CSM module made analyzing the flow within the combustor and interpreting the experimental data obtained from the shock-tunnel tests difficult.

The goal of the computational component of the project was to deal with the complexity of analyzing the flow within the module by building a code for the simulation of the three-dimensional supersonic flow. Presently, this code (named *sm_3d*)[6] is a space-marching flow solver for inviscid, supersonic flow. In the following sections, the code is described and applied to 1) the simulation of the flow within the CSM com-

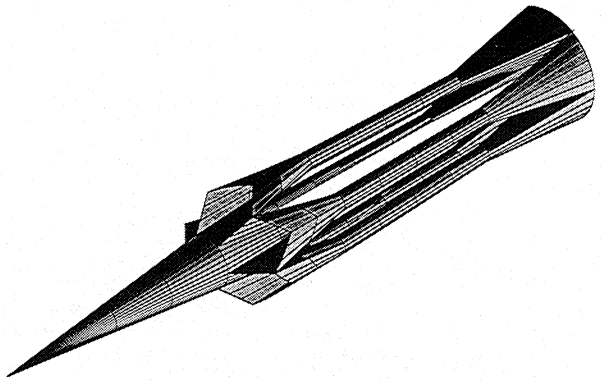

Fig. 1 Baseline design for the scramjet-powered stage. The conical forebody and the scramjet modules are shown with the cowl removed.

bustor, and 2) the optimization of a box-section thrust surface for three distributions of heating within the combustor.

Space-Marching Flow Solver

The finite volume formulation and the use of an upwinding technique enables *sm_3d* to capture shocks. This is important for the simulation of scramjet flows, where shocks are inevitably generated as the supersonic flow is processed by the inlet contraction, and where the curved walls of the duct make it difficult to estimate shock locations and strengths by inspection (or simple analysis).

The effects of combustion are modeled simply as a source term in the energy equation. Heat is added to individual cells based on a specified distribution, which is presently hard-coded for each case. This allows a direct study of the optimal distribution of heating, but does not consider the detailed mechanisms of fuel mixing and combustion. A chemical kinetics module has been built and will be added later.[7]

There are some other limitations to the solver. Because full three-dimensional flow solutions are to be computed relatively quickly on modest computers, a space-marching technique is employed that keeps only a few slices of flow data in memory. Srinivas[8] notes that the space-marching techniques require an order of magnitude less CPU time than time-marching schemes when computing two-dimensional flows. A similar gain is also expected for three-dimensional flows. Once the flow at the inlet plane is specified, the full solution is then obtained by starting at the inlet plane and marching along the duct, obtaining the steady-flow properties one slice at a time. This technique assumes that the flow is steady and, for the particular compressible-flow formulation used here, is supersonic along the duct. An implication of this assumption is that the ability to capture recirculation regions is sacrificed. Recirculation regions may be an important class of mechanisms for flameholding.

The version of the code described here does not include viscous effects; however, the code has been arranged to enable relatively straightforward inclusion of viscous terms at a later date. Although it is expected that viscous effects will be important in the design of full-sized combustors, inviscid flow solutions can be used to provide guidance on issues such as the placement of injectors for the optimal distribution of heat addition and the shape of thrust nozzles.

Another constraint on the current version of the code is that the duct geometry is discretized into a logically cubic grid of hexahedral cells. This allows the calculation of flow through a single duct of arbitrary shape or around a solid body such as a winged cone. However, it does not allow the calculation of the flowfield where there are multiple flow paths. Such a situation occurs with the simulation of a complete vehicle, where some of the flow passing over the forebody enters the scramjet modules while the rest passes over the cowl. For example, see the work by Wadawadigi et al.,[9] where multiple flow paths were considered for the tip-to-tail calculation of the flow about a generic hypersonic vehicle with airframe-integrated scramjet engines.

Formulation

The basic formulation of the solver is for a time-dependent compressible flow with the flow domain being discretized into an array of finite volume cells. This approach has been used in a number of other codes,[8,10] but it contrasts with codes based on the steady-flow formulation where the time derivatives do not appear.[11,12] Even though the time-dependent approach requires an iteration in time to reach steady flow at each station along the duct, it has the advantage that relatively large streamwise steps may be taken. This may be advantageous in difficult duct geometries where robust (and, consequently, expensive) grid generation schemes must be used.

Another aspect of the formulation that contrasts with most other space-marching codes is that the Cartesian form of the governing equations is retained in the code and the stored data. This approach has been used previously for blunt-body studies.[13] It leads to a simpler formulation when compared with formulations that transform the governing equations to computational space. However, a penalty of the present approach is that the code must handle the generalized cell geometry and the vector arithmetic.

The Euler equations in Cartesian coordinates can be expressed in vector form as

$$\frac{\partial}{\partial t}\int_V \boldsymbol{U}\,\mathrm{d}V + \int_S \bar{\boldsymbol{F}}\cdot\hat{\boldsymbol{n}}\,\mathrm{d}S = \int_V \boldsymbol{Q}\,\mathrm{d}V \tag{1}$$

where the algebraic vector of dependent flow variables is

$$\boldsymbol{U} = [\rho,\ \rho u_x,\ \rho u_y,\ \rho u_z,\ \rho E]^T \tag{2}$$

the inviscid flux vector is

$$\bar{\boldsymbol{F}} = \begin{bmatrix} \rho u_x \\ \rho u_x^2 + P \\ \rho u_y u_x \\ \rho u_z u_x \\ \rho E u_x + P u_x \end{bmatrix}\hat{\boldsymbol{i}} + \begin{bmatrix} \rho u_y \\ \rho u_x u_y \\ \rho u_y^2 + P \\ \rho u_z u_y \\ \rho E u_y + P u_y \end{bmatrix}\hat{\boldsymbol{j}} + \begin{bmatrix} \rho u_z \\ \rho u_x u_z \\ \rho u_y u_z \\ \rho u_z^2 + P \\ \rho E u_z + P u_z \end{bmatrix}\hat{\boldsymbol{k}} \tag{3}$$

and the source term is

$$\boldsymbol{Q} = [0,\ 0,\ 0,\ 0,\ q]^T \tag{4}$$

These equations specify the conservation of mass, three components of momentum, and total energy

$$E = e + 0.5(u_x^2 + u_y^2 + u_z^2) \tag{5}$$

in the control volume V bounded by the surface S. They are augmented by the equation of state, which relates the gas pressure to the local specific internal energy and density as

$$P = P(\rho, e) \tag{6}$$

For a calorically perfect gas, the following is used:

$$P = \rho(\gamma - 1)e \tag{7}$$

where $\gamma = C_p/C_v$ is the ratio of specific heats for the gas.

The conservation equations [Eqs. (1–4)] are applied to hexahedral cells, as shown in Fig. 2. The Cartesian coordinates (x, y, z) and the normalized (ξ, η, ζ) coordinate systems are shown. Note that the marching direction, ξ, is aligned with the supersonic flow direction. Cell-averaged data are associated

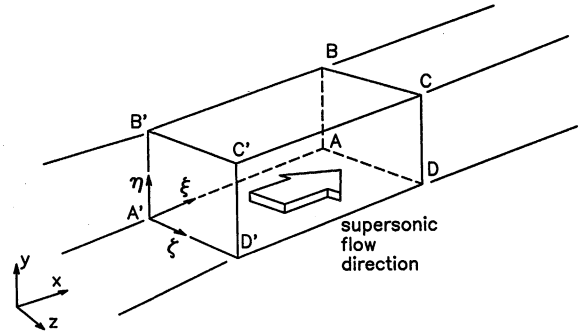

Fig. 2 Finite volume cell with coordinate directions and vertex labels.

with cell centers and the cells are indexed with *ix*, *iy*, and *iz* counters corresponding to the ξ, η, and ζ coordinate directions, respectively.

Flux Calculation

For the $ix - 1/2$ and $ix + 1/2$ interfaces, the assumption of supersonic flow in the *ix* coordinate direction makes the flux calculation trivial. Flow properties (ρ, u_x, u_y, u_z, e, and P) for interface $ix - 1/2$ are interpolated from the cell-centerd data in slices $ix - 2$, $ix - 1$, and ix, whereas flow properties for interface $ix + 1/2$ are extrapolated from the same cell-centered data. The interpolation or extrapolation is done separately for each of the flow variables and the estimated interface properties are simply combined to form the cell-interface fluxes given in Eq. (3).

The cross-stream interfaces $iy \pm 1/2$ and $iz \pm 1/2$ require a more robust flux calculation procedure so that oblique shocks within the flow can be captured without large oscillations in the flow properties. Here, a Godunov-type scheme is used based on the generalized MUSCL reconstruction[14] of the flow properties within the slice, followed by the application of a Riemann solver to resolve differences at each of the interfaces.

Prior to interpolation, boundary conditions are applied around the duct walls by setting up a layer of ghost cells (two deep) along each boundary. Presently, only the slip-wall (or tangency) boundary and the supersonic-inflow boundary conditions are available. The tangency condition is imposed by setting all of the scalar quantities within the ghost cells equal to those just inside the boundary. The velocity is set by rotating the velocity vector into a local frame of reference, copying the two tangential velocity components, and negating the normal component. For external flows, a supersonic-inflow condition may be applied by simply copying the freestream quantities into the ghost cells. The reconstruction procedure may then be applied (uniformly) across the entire slice.

Space-Marching and Pseudotime Iteration

Relative to a time-marching code for three-dimensional flow, the amount of data that needs to be stored for a space-marching code is small. Enough data are stored to define the geometry and flow state of the currently active slice of the flowfield along with two extra slices of cell-centered data. This enables high-order reconstruction in the streamwise direction. Although the code is intended for computing three-dimensional flows, two-dimensional flows may be studied by collapsing one of the cross-stream directions to a minimum of two active cells and specifying parallel walls normal to this coordinate direction. The required minimum of two active cells imposes a penalty in both memory and CPU time required to compute two-dimensional flows, but it does simplify the coding within *sm_3d*.

The solution at the current slice is first guessed by extrapolating from the slice immediately upstream. The semidiscrete form of conservation equation is then integrated in time until steady state is achieved. Note that this time iteration does not represent a physical evolution of the flow and, because a time-accurate solution is not required, a simple explicit time-stepping scheme is used.

When checking to see if the flow has reached a steady state across the whole slice, the following convergence criteria are used:

1) Relative changes in density for a time step are less than a specified tolerance (typically 10^{-4}).

2) At least five flow lengths have passed through the slice.

3) A maximum number of time steps has not been exceeded (typically 100).

A crude rule-of-thumb is that these criteria force about 30 iterations per slice for relatively easy flows, whereas strong shock or expansion fans may require 80 iterations or more. Once a steady-state solution is obtained for the current slice, pointers to the data slices are exchanged.

The CPU time required per active cell per time step is in the range of 250–350 μs on an IBM RISC-6000 workstation. Because this estimate includes the time for data initialization and file I/O, the CPU time required for a specific case will depend on the size of the grid.

Boundary Definition and Grid Generation

The three-dimensional grid is generated one vertex slice at a time from information about the four duct boundaries. Given a particular value of ξ, the geometry module generates arrays of vertices in the (η, ζ) plane as shown in Fig. 3. Presently, the code requires boundary information in the form of parameterized interpolation points $\bar{P}_{DA}(\zeta)$, $\bar{P}_{CB}(\zeta)$, $\bar{P}_{DC}(\eta)$, and $\bar{P}_{AB}(\eta)$ for $0 \le \eta \le 1$ and $0 \le \zeta \le 1$. Transfinite interpolation (or a Coons patch[15]) is then used to obtain the position of the vertex as

$$\bar{P} = (1-\eta)\bar{P}_{DA} + \eta\bar{P}_{CB} + (1-\zeta)\bar{P}_{DC} + \zeta\bar{P}_{AB} - (1-\eta)(1-\zeta)\bar{P}_{D} - (1-\eta)\zeta\bar{P}_{A} - \eta(1-\zeta)\bar{P}_{C} - \eta\zeta\bar{P}_{B} \quad (8)$$

where $\bar{P}_A$ to $\bar{P}_D$ are the positions of the corners of the duct cross section. Note that these points need not be coplanar in the Cartesian coordinate system and that the corners need not be corners in a physical sense. For example, each of the grids in the Cartesian coordinate system in Fig. 3 may be mapped to a square in the (η, ζ) plane. The circular grid required for the CSM combustor section and the grids downstream of the combustor are examples of difficult cross-sectional geometries because the cells in the (rounded) corners tend to collapse and have little volume. In these cases, a Laplacian smoother is used to assist the algebraic grid generator.

The arrays of vertices on the boundaries in the (η, ζ) plane are generated by the geometry module in three different ways, depending on the complexity of the duct geometry. Box-section grids are generated using straight-line segments. The problem parameter file contains a series of point coordinates determining the position of endpoints of the line segments that define the four duct boundaries. Given a particular ξ value, the corner points of the cross section ($\bar{P}_A$ to $\bar{P}_D$) can be interpolated

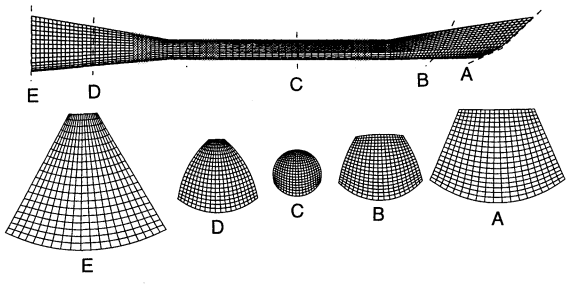

Fig. 3 Computational grids for several slices through a scramjet duct.

from the line segments. The vertex points that define the boundaries of the duct cross section are then interpolated along each of these lines.

For a smoother variation in duct cross section, the line segments defining the corners of the duct cross sections can be replaced by Bezier curves.[15] The point coordinates in the parameter file then become the polygon points for the Bezier curves, and the corner points $\bar{P}_A$ to $\bar{P}_D$ are points on these Bezier curves. This form of boundary description is convenient for shape optimization because 1) there is a simple and intuitive relationship between the polygon point positions and the resultant Bezier curve, and 2) the Bezier curve is always well behaved.

For more complex geometries, where the cross-sectional shape of the duct is not quadrilateral, B-spline surfaces are used. The four walls of the duct are defined by four B-spline surface patches and the point-coordinate data in the parameter file are replaced by four control-net files. The B-spline module[16] calculates the edges of the cross section for a given value of ξ. The internal vertices of the grid are then calculated algebraically as done for the box-section grids. This permits shape transition cross sections to be modeled in a relatively straightforward manner because B-spline surfaces can be fitted to any continuous surface. In this study, a B-spline surface description is used for the three-dimensional CSM scramjet module.

Optimization Procedure

This study couples the computational fluid dynamics (CFD) solver to a Nelder–Mead optimization procedure to find an optimum thrust surface contour for a two-dimensional scramjet combustor and exhaust.[17,18] Other investigators have used the technique of coupling a CFD code and an optimizer to design aerodynamic bodies. For example, Korte et al.[19] used a gradient mapping technique to find the optimal shape of a scramjet inlet and a least-squares approach to design hypersonic wind-tunnel nozzles.[20] The optimization of a simplified scramjet thrust surface was performed by Baysal and Eleshaky,[21] using a quasianalytical optimization technique that involved finding gradients of objective functions. They restricted their CFD analysis to inviscid, two-dimensional flows in which the inflow conditions were uniform. In another scramjet study, McQuade et al.[22] investigated engine/airframe integration by coupling an optimization procedure to a set of simplified flow problems in which the CFD analyses were limited to one- and two-dimensional flows. A more recent study by Sabean and Lewis[23] used commercial optimization and CFD tools to optimize the shape of an axisymmetric scram accelerator. The flows were assumed to be inviscid with the fuel and oxidizer premixed; however, a two-step finite rate chemistry model was used to determine the heat release. As well as these supersonic/hypersonic examples, optimization has also been used for aerofoil design in the subsonic and transonic regime.[24,25] For the present study, the simplifications of inviscid, nonreacting flows will be retained. However, depending on the distribution of heat in the combustor, the flows may be three dimensional.

The Nelder-Mead optimization procedure[17,18] was chosen for this study because it is robust and because it does not require evaluation of the derivatives of the objective function, it allows a simple coupling to the CFD solver. The objective function is selected to maximize the axial thrust, and the design parameters are mapped to the control points of the Bezier curve, which defines the shape of the thrust surface. For a vector of n design parameters, the optimizer forms a simplex of $n + 1$ sample points in parameter space and then takes a number of steps, moving away from the worst objective value at each step. For each evaluation of the objective function, the duct geometry is derived from the current values of the parameter vector and the space-marching flow solver is called as a subroutine. During the computation of each flow solution, specific data (such as the integrated pressure forces along the duct walls) are saved and later returned to the calling routine.

Flow in a Three-Dimensional Scramjet Module

An application of the code to the simulation of three-dimensional flow in just one of the six scramjet modules from the launch vehicle of Fig. 1 is now considered. The CSM module (shown in Fig. 4) is the third in the series of scramjet motors built for the experimental study.[26] The module is fabricated from a fiber-reinforced plastic and has a relatively complex three-dimensional geometry, which is the result of a number of geometric constraints. The first constraint arises because each of the six modules on the launch vehicle should ingest its full share of the shock layer generated by the conical forebody. The front projection of the module's inlet must, therefore, occupy a sector of a circle. The shape of the exhaust nozzle is similarly constrained. To make the inlet self-starting, the sidewalls are swept back from the oncoming flow at 45 deg, and the cowl surface is recessed even farther. Between the compression inlet and the thrust nozzle, the combustors are

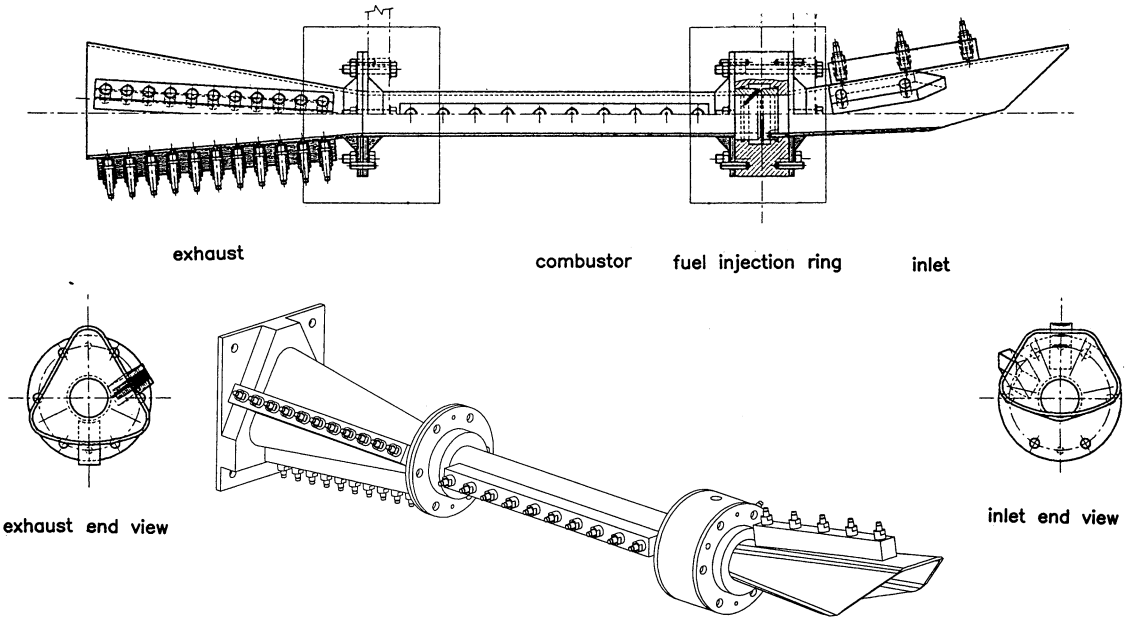

Fig. 4 Front, side, and rear views of the CSM scramjet module.

given a circular cross section to achieve a high strength-to-weight ratio.[27] Overall, the module is similar to that used in the SCRAM-MOD 1 missile described by Billig.[28] However, an isolator is not included as the CSM module is intended for supersonic combustion only.

The inlet flow condition for the simulation has been selected to approximate the experimental flow condition.[26] The air test gas is assumed to be perfect with gas constants $R = 287$ J/(kg K) and $\gamma = 1.4$. Gas enters the compression inlet with properties $P = 10.0$ kPa, $\rho = 0.085$ kg/m^3, and $u = 2375$ m/s at an angle of 0.5 deg to the leading-edge surface of the inlet, $T = 410$ K, and $M = 5.85$. Energy is uniformly added to a block of cells to simulate hydrogen combustion. The location of the heating zone is centered on $x = 0.325$ m with a half-length of 0.025 m. Within this heating zone, 1.22 MJ/s is added to the flow, giving an effective equivalence ratio of 0.53. The equivalence ratio is based on the assumptions that complete combustion occurs and that the heating value of complete hydrogen–oxygen combustion is 90 MJ/kg of gaseous hydrogen.[29] In arriving at this heating value, we also assume that the average combustor temperature is 2000 K.

Figures 5 and 6 compare the simulated and measured wall pressures within the scramjet module. One set of data is for a no-fuel shot and the other set is for a fuel equivalence ratio of approximately 0.5. Also shown in these figures are quasi-one-dimensional results for the same heat addition.

The quasi-one-dimensional calculation is based on the axial distribution of the cross-sectional area of the duct, and the governing equations are derived from the integration of the conservation equations for generalized compressible pipe flow with Rayleigh-line heat addition.[30] For a given inflow condition, heat addition distribution, and cross-sectional area distribution, a small step of length δx is taken along the duct, and the increments in flow properties are computed as

$$\frac{\delta u}{u} = \frac{-1}{1 - M^2}\left[\frac{\delta A}{A} - \frac{\delta q}{C_p T}\right]$$

$$\frac{\delta T}{T} = \frac{\delta q}{C_p T} - (\gamma - 1)M^2 \frac{\delta u}{u} \tag{9}$$

$$\frac{\delta p}{p} = \frac{\delta T}{T} - \frac{\delta u}{u} - \frac{\delta A}{A}$$

where

$$\delta q = \frac{dq}{dx}(x) \cdot \delta x$$

$$\delta A = A(x + \delta x) - A(x) \tag{10}$$

The secondary flow variables can be obtained from the relations

$$\rho = p/RT, \qquad a = (\gamma RT)^{1/2}, \qquad M = u/a \tag{11}$$

These equations are integrated along the length of the duct. For supersonic flows, this integration procedure will work as long as sonic conditions are not passed.

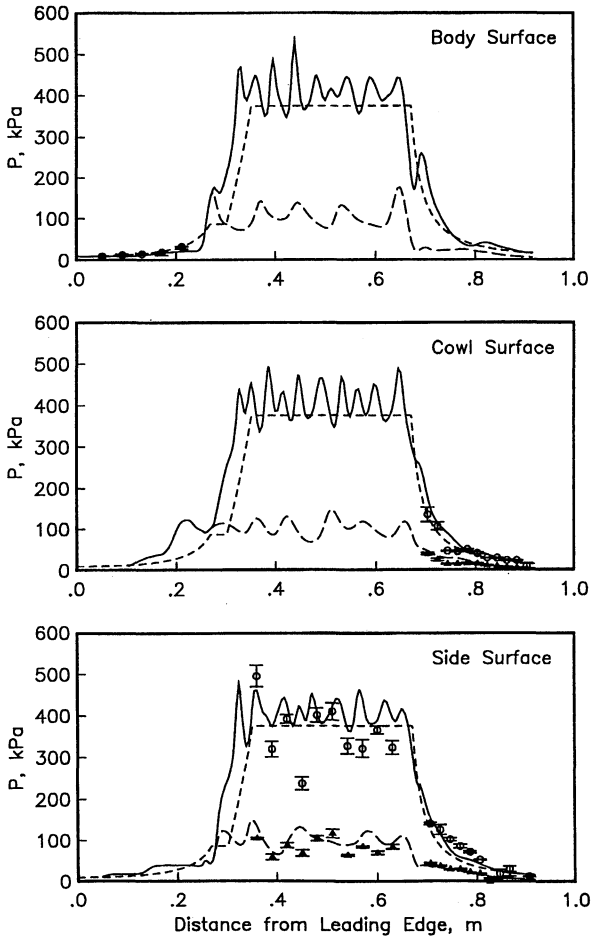

Fig. 5 Comparison of simulated and measured wall pressures within the CSM module. The long dashed line denotes flow without heat addition, the solid line indicates flow with heat addition, and the short dashed line represents quasi-one-dimensional flow with heat addition. The symbols denote measured pressures, and the bars indicate the variation in pressure signal during the test time.

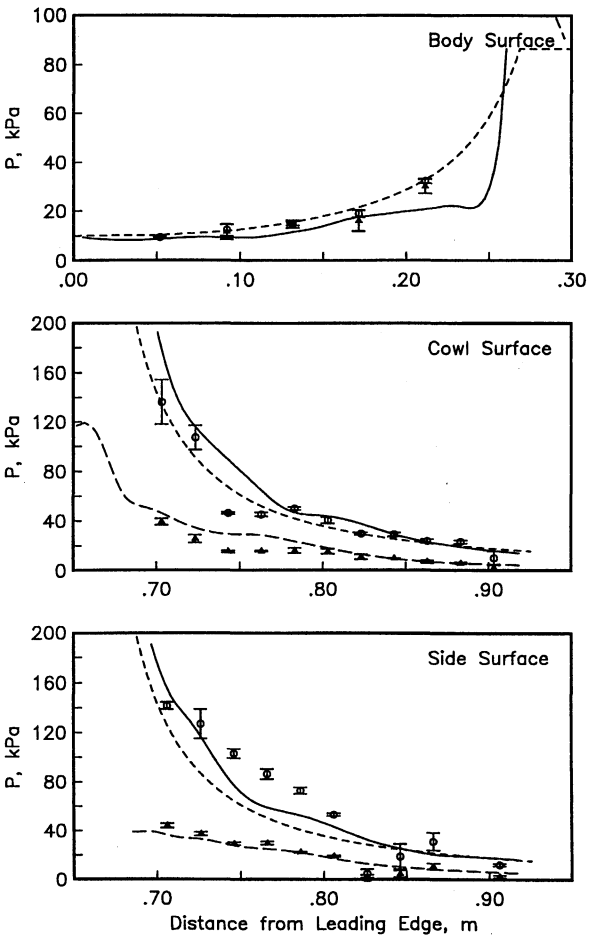

Fig. 6 Expanded view of the simulated and measured wall pressures in the compression inlet and thrust nozzle of the CSM module.

Despite a number of differences in detail, the comparison between the experimental data and the computed pressure levels is reasonable. Viscous and turbulence effects have yet to be included in the simulations and these effects are expected to influence the data toward the end of the compression inlet ($x \simeq 0.2$ m), within the combustor, and near the beginning of the thrust nozzle ($x \simeq 0.75$ m). Also, the experimental data are preliminary and genuine error bars are not shown. Instead, the bars indicate the variation of the filtered pressure signal during the test flow time. To estimate the thrust produced by the module, pressure is integrated over the internal surfaces. Although skin friction losses are omitted, the inviscid drag because of the conical forebody is deducted. The net thrust computed for three-dimensional flow with an equivalence ratio of 0.53 is then 280 N and the corresponding specific impulse, I_{sp} = thrust/($g\dot{m}_{fuel}$), for the module is 2100 s.

The constant-area combustor is designed to ensure vigorous combustion in the test flow conditions available in the T4 shock tunnel. The result is a compromise, where the combustor chokes when all of the heat is released for a fuel equivalence of unity. Figure 7 shows a graph of thrust vs heat release/equivalence ratio and thermal choking limits for both three-dimensional and quasi-one-dimensional simulations. The thermal choking limits represent the points where calculations are terminated as a result of sonic flow. Quasi-one-dimensional simulations show the onset of choking at higher equivalence ratios. This is because of the three-dimensional calculations terminating with the appearance of local sonic regions, whereas the one-dimensional calculations terminate only when the whole duct approaches sonic conditions. The three-dimensional flow simulations are terminated at an effective equivalence ratio of 0.71, whereas the one-dimensional simulations are taken to 0.85. These values are consistent with the experimental results, where a transient choking effect was seen for a fuel equivalence ratio of 0.85.[26]

Specific impulses are also calculated for the same heat release and combustor configurations as shown in Fig. 8. For the three-dimensional simulation, there is a drop in specific impulse as the heat release is reduced. It is possible that for the low-heat-release cases, there is a relatively large error in the net thrust estimate, which is further magnified in the calculation of the specific impulse. This was investigated further by analyzing solutions produced by the code for different grid resolutions. The original grid was halved, doubled, and quadrupled in size, and the maximum drag value produced prior to expansion was compared. Across the four solutions, there was a 0.7 N (0.6%) uncertainty in the drag estimate of 120 N. The net thrust may then have an uncertainty of 1.4 N, which, for low heat additions, represents a relative error of up to 7%. For moderate heat additions, the uncertainty in net thrust is approximately 1%.

To enable operation of the scramjet module at a fuel equivalence ratio of unity, a diverging combustor is considered, such that its circular cross section is expanded by a three-deg half-angle over the heat release zone. The divergence is started at the junction of the inlet and combustor, and terminated at an axial position of $x = 0.424$ m. The heat addition is started at a point just after the beginning of the divergence and finishes just before $x = 0.424$ m. The divergence reduces both the temperature and the pressure rises over the heat addition zone and allows a larger heat addition while maintaining supersonic flow. The diverging combustor can achieve a net thrust of 475 N (at $\phi = 1$) compared with the maximum thrust of 379 N (at $\phi = 0.71$) for the constant area combustor.

There is, however, a thermodynamic penalty associated with adding heat in a diverging duct. For a given heat addition, the diverging combustor produces a lower net thrust (Fig. 7) and a corresponding lower specific impulse (Fig. 8). For a fuel equivalence ratio of 0.5, the thermodynamic cycles of both combustors are shown in Fig. 9. The open thermodynamic cycle for the nondiverging combustor engine is 1-2-3-4 and for the diverging combustor engine it is 1-2-2′-3′-4′. The process of adding heat while undergoing an expansion results in a larger increase in entropy and a corresponding increase in heat rejected in the exhaust stream.

This inviscid analysis has so far ignored the other benefits of minimizing the combustor temperature and pressure rise. It is expected that there are benefits to be gained in avoiding inhibition of the formation of combustion products at high temperatures and in avoiding the larger wall shear stresses that

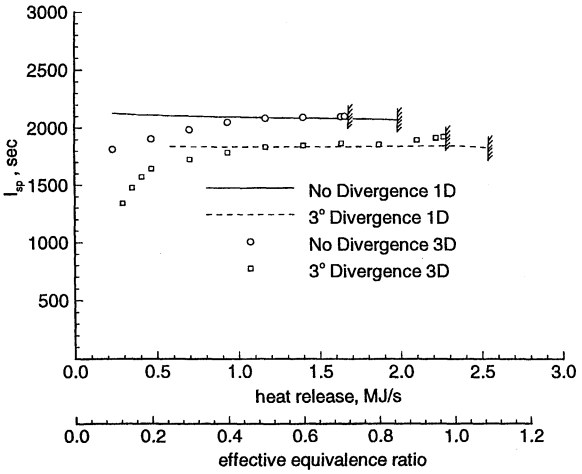

Fig. 8 Simulated specific impulse values for varying heat release with sonic flow limits.

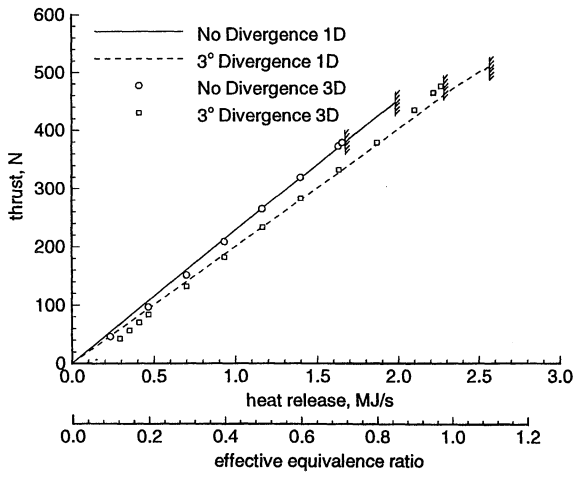

Fig. 7 Simulated thrust values for varying heat release with sonic flow limits.

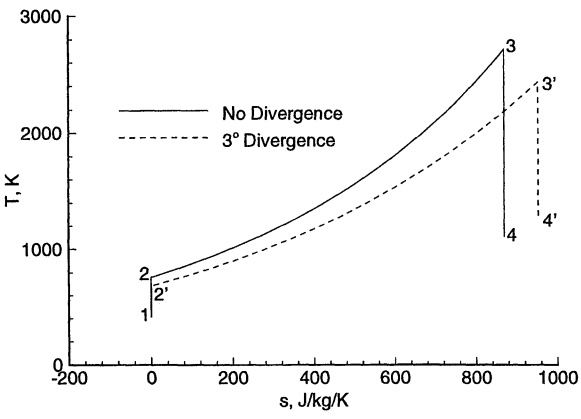

Fig. 9 Temperature vs entropy change for two different scramjet designs. The reference entropy is taken to be the freestream value.

would accompany high temperatures and high-pressure combustor flows.

Optimization of a Thrust Nozzle

For an optimization example, a simpler two-dimensional scramjet is considered as shown in Fig. 10. The inlet consists of a pair of straight compression surfaces with a half-angle of 11 deg and a cowl aligned with the vehicle (x) axis. The combustor has a constant area and is also aligned with the vehicle axis. This is followed by a nozzle which, for the baseline design, consists of a straight thrust ramp with an inclination of 20 deg to the axis. The width of the vehicle (in the z direction) is set to 1 m.

The nominal flight Mach number is 15 at an altitude of 30,000 m. The freestream conditions are P = 1144 Pa, u_x = 4440 m/s, and T = 218 K. Air is processed by two oblique shocks and enters the combustor at M = 5.4 and at a pressure of 101 kPa. The inlet geometry is arranged such that the first shock intersects the leading edge of the cowl and the second (reflected) shock is canceled at the corner starting the combustor. Assuming a nominal heating value of 90 MJ/kg for hydrogen fuel, heat is added to the flow in the combustor at the rate of 203 MJ/s to give an approximately stoichiometric fuel–air mixture. This heat is distributed uniformly throughout the combustor over $4.92 \leq x \leq 5.22$ m. It results in a decrease in Mach number to 2.72 and an increase in static pressure to 370.3 kPa prior to the expansion of the flow over the thrust ramp. Figure 10 shows the pressure contours within the scramjet module for these flight conditions. The simulated net thrust is 35.75 kN per module and the vehicle specific impulse is 859 s. If the flow through the thrust nozzle is assumed to be quasi-one-dimensional, the specific impulse would be 1135 s for this operating condition.

For the nozzle optimization study, only the combustor–nozzle section of the scramjet vehicle is considered. The duct corners are defined with a set Bezier curves of degree 7. The polygon points defining the ramp surface are distributed in the x direction at x = 4.923, 5.109, 5.456, 5.723, 6.354, 6.984, 7.615, and 8.245 m. The y positions of the polygon points x = 6.354, 6.984, and 7.615 m are used as the optimization parameters, whereas the objective function is formulated as a scaled specific impulse for the scramjet nozzle alone. Note that the nozzle cross sections remain rectangular.

The simplex routine is then allowed to perturb the nozzle shape to achieve an optimum specific impulse. This optimum is usually achieved within 35–45 evaluations of the objective function, with one flow solution computed per function evaluation. Figure 11 shows the pressure contours for the straight-ramp nozzle, the initial unoptimized Bezier nozzle, and the optimized Bezier nozzle. The specific impulse for the optimized nozzle alone is 1666 s and for the full vehicle with the optimized nozzle is 927 s. This is a 8% improvement over the straight-ramp thrust surface and a 16% improvement over the unoptimized Bezier thrust surface. One might expect the initial Bezier surface to have a higher performance than the straight-ramp case because of a longer nozzle providing more opportunity for wave cancellation. However, the unoptimized Bezier thrust surfaces sees a lower pressure on the later part of the thrust surface than the corresponding segments of the straight ramp. The integrated effect is a lower axial thrust for the unoptimized Bezier ramp. The same mechanism can be used to explain the improved performance of the optimized surface. For this nozzle, the plotted contours indicate that, although the pressure initially decreases more rapidly than for the unoptimized nozzle, a relatively high pressure is maintained on the thrust surface for 6.5 m $\leq x \leq$ 8 m.

To check the sensitivity of the optimum shape to the specific distribution of heat within the combustor, two other variations of heat addition are considered, as shown in Fig. 12. The first variation distributes the heat in a horizontal volume spanning the combustor and simulates the nominally two-dimensional scramjet models that have fuel-injection struts, which span the full width of the combustor. The second variation adds the heat at four round jets equally spaced across the combustor. This

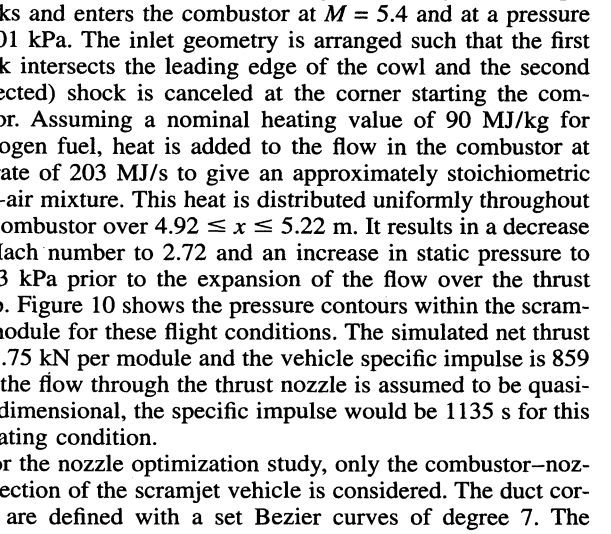

Fig. 10 Baseline two-dimensional scramjet vehicle with a combustor height of 82 mm.

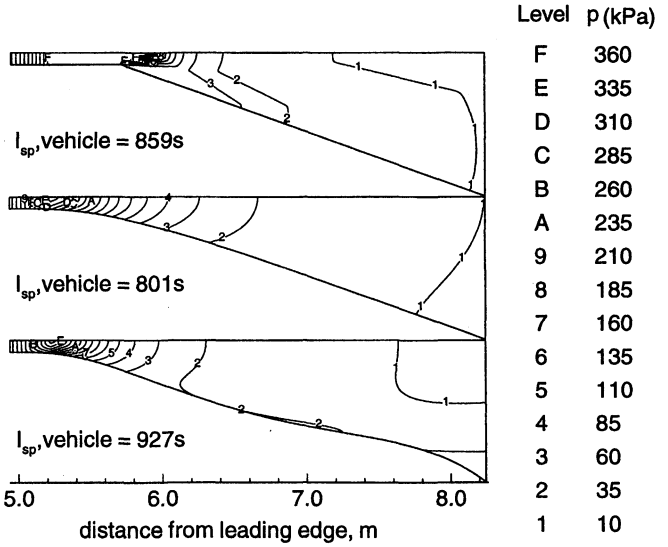

Fig. 11 Pressure contours for the straight ramp, initial unoptimized Bezier, and optimized Bezier nozzles.

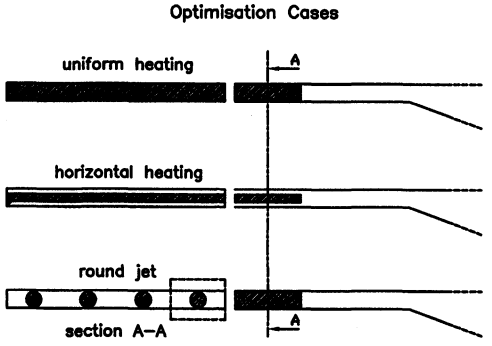

Fig. 12 Heat distributions for uniform, horizontal jet, and round jet heating.

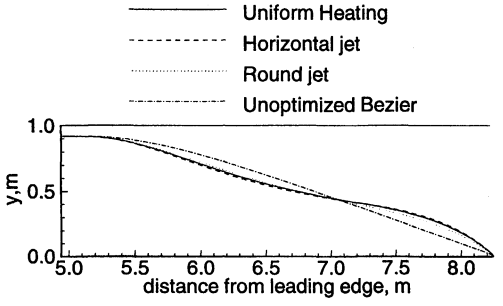

Fig. 13 Optimal thrust surfaces for a fuel equivalence ratio of 0.5 with uniform heating, horizontal-jet, and round-jet heating of the flow through the combustor. Also shown is the initial unoptimized Bezier surface.

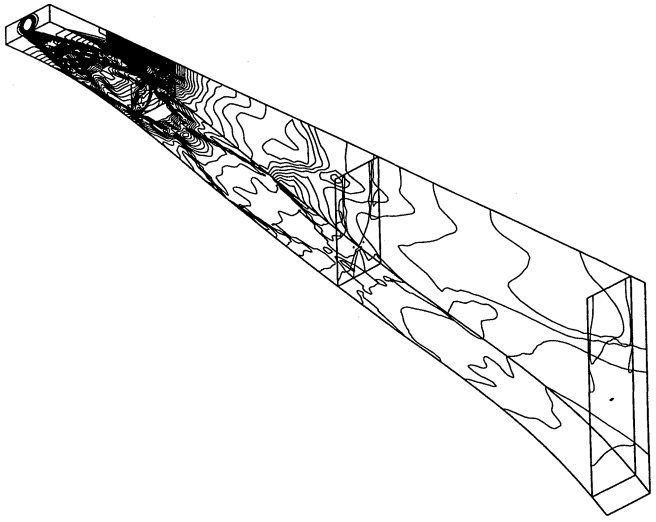

Fig. 14 Pressure contours within one-quarter of the thrust nozzle for the round-jet heating. Contours start at 6 kPa up to 564 kPa, in 6 kPa increments.

arrangement simulates fuel injection via a set of discrete orifice injectors and results in a fully three-dimensional flowfield within the combustor and nozzle. For the same initial duct geometry as for uniform heat addition simulation, but with an equivalence ratio of 0.5 (heat addition of 103 MJ/s), the optimization procedure produces the final thrust surface profiles shown in Fig. 13. There is very little difference between the profiles and performance of each of the nozzles when run with the alternative heat distributions. This result agrees with the observation made by Broadbent,[31] that the propulsive efficiency is not very sensitive to the precise distribution of heat.

Figure 14 shows the pressure contours on the nozzle walls for the round-jet heating. The complexity of this figure highlights the three-dimensional nature of the resulting flowfield.

Concluding Remarks

It has been shown that the space-marching code, *sm_3d*, provides reasonable solutions for inviscid flows in three-dimensional geometries, which are representative of scramjet modules. The study of the CSM scramjet illustrated the thermodynamic compromise between 1) the large pressure and temperature rises associated with adding heat in a constant area duct, and 2) the extra entropy rise (and accompanying performance loss) when adding heat in a diverging combustor.

The code is also capable of optimizing the shape of the scramjet modules for arbitrary fuel-heating distributions. Although it appears to be relatively easy to get good performance out of just about any nozzle for the inviscid flow of an ideal gas, it would be expected that there will be more significant and realistic performance constraints when viscous, mixing, and finite rate chemical effects are included. For example, the performance of a straight-ramp nozzle can be improved by increasing the nozzle length (and approaching a quasi-one-dimensional flow expansion). If viscous effects were to be added, there would be a significant thrust and heat transfer penalty associated with increasing the wetted length. To promote the formation of combustion products, the flow can be partially expanded while in the combustor; however, mixing and finite rate chemical reactions will impose a penalty for short combustors with rapid expansions. Expanding too quickly after injection will effectively extinguish the flame and, thus, reduce nozzle performance. In future work, the optimization of three-dimensional scramjet geometries (as used for the CSM module) will be studied for more realistic flows, which include the effects of viscosity, turbulence, mixing, and finite rate chemistry.

Acknowledgments

This computational study has evolved as part of a Collaborative Research Project sponsored by the Australian Research Council, Grant AM9180142. The industrial partners were Australian Defence Industries, Ltd. (for scramjet manufacture) and WBM Pty, Ltd. (for shock-tunnel testing). Other people involved in the project were Michael Wendt [University of Queensland (UQ)]; Conrad Stacey (WBM); Ray Stalker (UQ); Ken Davis [Australian Defence Industries (ADI)]; Malcolm Peck (ADI); and Colin Beech, Brian Loughrey, Bob Gammie, Ken Dudson, Leon Prucha, and Kevin Austin (UQ).

References

[1]Stalker, R. J., "Scaling Laws and the Launch Vehicle Market," Seventh National Space Engineering Symposium, Canberra, Australia, Sept. 1992.

[2]Covell, P. F., Wood, R. M., Bauer, S. X., and Walker, I. J., "Configuration Trade and Code Validation Study on a Conical Hypersonic Vehicle," AIAA Paper 88-4505, Sept. 1988.

[3]Northam, G. B., and Anderson, G. Y., "Supersonic Combustion Ramjet Research at Langley," AIAA Paper 86-0159, Jan. 1986.

[4]Paull, A., Stalker, R., and Mee, D., "Scramjet Thrust Measurement in a Shock Tunnel," *Aeronautical Journal*, Vol. 99, No. 984, 1995, pp. 161–163.

[5]Stalker, R., and Morgan, R., "The University of Queensland Free Piston Shock Tunnel T4—Initial Operation and Preliminary Calibration," 4th National Space Engineering Symposium (Adelaide, Australia), Inst. of Engineers, Australia, July 1988.

[6]Jacobs, P. A., "A Space-Marching Euler Solver for Supersonic Flow in a Three-Dimensional Geometry," Dept. of Mechanical Engineering, Rept. 2/95, Univ. of Queensland, Brisbane, Australia, Jan. 1995.

[7]Craddock, C. S., "A Quasi-One-Dimensional Space-Marching Flow Solver with Finite Rate Chemical Effects," Dept. of Mechanical Engineering, Rept. 7/96, Univ. of Queensland, Brisbane, Australia, April 1996.

[8]Srinivas, K., "An Expicit Spatial Marching Algorithm for Navier-Stokes Equations," *Computers and Fluids*, Vol. 21, No. 2, 1992, pp. 291–299.

[9]Wadawadigi, G., Tannehill, J. C., Lawrence, S. L., and Edwards, T. A., "Three-Dimensional Computation of the Integrated Aerodynamic and Propulsive Flowfields of a Generic Hypersonic Space Plane," AIAA Paper 94-0633, Jan. 1994.

[10]Siclari, M. J., and Del Guidice, P., "Hybrid Finite Volume Approach to Euler Solutions for Supersonic Flows," *AIAA Journal*, Vol. 28, No. 1, 1990, pp. 66–74.

[11]Korte, J. J., and McRae, D. S., "Explicit Upward Algorithm for the Parabolized Navier-Stokes Equations," AIAA Paper 88-0716, Jan. 1988.

[12]Korte, J. J., "An Explicit Upwind Algorithm for Solving the Parabolized Navier-Stokes Equations," NASA TP 3050, Feb. 1991.

[13]Rizzi, A. W., and Inouye, M., "Time-Split Finite-Volume Method for Three-Dimensional Blunt-Body Flow," *AIAA Journal*, Vol. 11, No. 11, 1973, pp. 1478–1485.

[14]Anderson, W. K., Thomas, J. L., and Van Leer, B., "A Comparison of Finite Volume Flux Vector Splittings for the Euler Equations," AIAA Paper 85-0122, Jan. 1985.

[15]Rogers, D. F., and Adams, J. A., *Mathematical Elements for Computer Graphics*, 2nd ed., McGraw–Hill, New York, 1990.

[16]Craddock, C., "B-Spline Surfaces for CFD Grid Generation," Dept. of Mechanical Engineering, Rept. 1/95, Univ. of Queensland, Brisbane, Australia, Jan. 1995.

[17]Nelder, J. A., and Mead, R., "A Simplex Method for Function Minimization," *Computer Journal*, Vol. 7, 1965, pp. 308–313.

[18]O'Neill, R., "Algorithm AS47. Function Minimization Using a Simplex Algorithm," *Applied Statistics*, Vol. 20, No. 3, 1971, pp. 338–345.

[19]Korte, J. J., Singh, D. J., Kumar, A., and Auslender, A. H., "Numerical Study of the Performance of Swept, Curved Compression Surface Scramjet Inlets," *Journal of Propulsion and Power*, Vol. 10, No. 6, 1994, pp. 841–847.

[20]Korte, J., "Aerodynamic Design of Axisymmetric Hypersonic Wind-Tunnel Nozzles Using a Least-Squares/Parabolized Navier-Stokes Procedure," *Journal of Spacecraft and Rockets*, Vol. 29, No. 5, 1992, pp. 685–691.

[21]Baysal, O., and Eleshaky, M., "Aerodynamic Design Optimization Using Sensitivity Analysis and Computational Fluid Dynamics," *AIAA Journal*, Vol. 30, No. 3, 1992, pp. 718–725.

[22]McQuade, P. D., Eberhardt, S., and Livne, E., "CFD-Based Aerodynamic Approximation Concepts Optimization of a Two-Dimensional Scramjet Vehicle," *Journal of Aircraft*, Vol. 32, No. 5, 1995, pp. 262–269.

[23]Sabean, J. W., and Lewis, M. J., "Performance Optimization of a Supersonic Combustion Ram Accelerator Projectile," *Journal of Propulsion and Power*, Vol. 13, No. 5, 1997, pp. 592–600.

[24]Kuruvila, G., Ta'asan, S., and Salas, M., "Airfoil Design and Optimization by the One-Shot Method," AIAA Paper 95-0478, Jan. 1995.

[25]Eleshaky, M., and Baysal, O., "Airfoil Shape Optimization Using Sensitivity Analysis on Viscous Flow Equations," *Journal of Fluids Engineering*, Vol. 115, No. 1, 1993, pp. 75–84.

[26]Wendt, M. N., and Jacobs, P. A., "Modular Composite Scramjet Motor (C.S.M) Testing," Dept. of Mechanical Engineering, Rept. 2/96, Univ. of Queensland, Brisbane, Australia, Feb. 1996.

[27]Pinckney, S. Z., "Rectangular Capture Area to Circular Combustor Scramjet Engine," NASA TM 78657, March 1978.

[28]Billig, F. S., "SCRAM-A Supersonic Combustion Ramjet Missile," AIAA Paper 93-2329, June 1993.

[29]Chase, M. W., *JANAF Thermochemical Tables*, American Inst. of Physics, New York, 1985.

[30]Zucrow, M. J., and Hoffman, J. D., *Gas Dynamics*, Vol. 1, Wiley, New York, 1976.

[31]Broadbent, E. G., "Flows with Heat Addition," *Progress in Aerospace Science*, Vol. 17, No. 2, 1976, pp. 93–108.